

# Aluminum foam integral armor: a new dimension in armor design

Bazle A. Gama<sup>a,b,\*</sup>, Travis A. Bogetti<sup>d</sup>, Bruce K. Fink<sup>d</sup>, Chin-Jye Yu<sup>e</sup>, T. Dennis Claar<sup>e</sup>,  
Harald H. Eifert<sup>e</sup>, John W. Gillespie Jr.<sup>a,b,c</sup>

<sup>a</sup> Center for Composite Materials (CCM), University of Delaware, Newark, DE 19716, USA

<sup>b</sup> Department of Materials Science & Engineering, University of Delaware, Newark, DE 19716, USA

<sup>c</sup> Department of Civil & Environmental Engineering, University of Delaware, Newark, DE 19716, USA

<sup>d</sup> US Army Research Laboratory, Aberdeen Proving Ground, MD 21005, USA

<sup>e</sup> Fraunhofer USA Center–Delaware (FC–DE), Newark, DE 19716, USA

---

## Abstract

Closed-cell aluminum foam offers a unique combination of properties such as low density, high stiffness, strength and energy absorption that can be tailored through design of the microstructure. During ballistic impact, the foam exhibits significant non-linear deformation and stress wave attenuation. Composite structural armor panels containing closed-cell aluminum foam are impacted with 20-mm fragment-simulating projectiles (FSP). One-dimensional plane strain finite element analysis (FEA) of stress wave propagation is performed to understand the dynamic response and deformation mechanisms. The FEA results correlate well with the experimental observation that aluminum foam can delay and attenuate stress waves. It is identified that the aluminum foam transmits an insignificant amount of stress pulse before complete densification. The ballistic performance of aluminum foam-based composite integral armor (CIA) is compared with the baseline integral armor of equivalent areal-density by impacting panels with 20-mm FSP. A comparative damage study reveals that the aluminum foam armor has finer ceramic fracture and less volumetric delamination of the composite backing plate as compared to the baseline. The aluminum foam armors also showed less dynamic deflection of the backing plate than the baseline. These attributes of the aluminum foam in integral armor system add a new dimension in the design of lightweight armor for the future armored vehicles. © 2001 Elsevier Science Ltd. All rights reserved.

**Keywords:** Closed-cell aluminum foam; Composite integral armor (CIA); Stress wave propagation; Multi-step processing; Ballistic testing; Dynamic deflection

---

## 1. Introduction

The US Army has established and documented requirements for lightweight structural armors that exhibit significant advancements in the integration of ballistic and structural performance [1]. Fig. 1 depicts the historical development of armors for 0.50 cal heavy machine gun threat demonstrating continuous improvements; yet significant challenges exist in further reducing the areal-density by half. Such a reduction in armor weight requires the integration of new materials through micro-structural design, improved understanding of stress wave propagation at dissimilar material interfaces, optimization of multiple competing performance metrics, and innovative armor concepts.

The development of lightweight ceramic–metal armor is based on the pioneering work of Wilkins et al. [2], who developed ceramic–aluminum armor system and later [3,4] studied the penetration mechanism of such armor. A comprehensive summary of lightweight armor development is given by Viechnicki et al. [5]. It is now well known that the high hardness ceramic deforms and erodes the penetrator through a complex brittle fracture mechanism of the ceramic and has been investigated by researchers over last two decades. While the ceramic fracture process absorbs insignificant amount of energy (~0.2%) of the projectile, a major portion (20–40%) is absorbed by the deformation processes of the backing plate. The rest of the kinetic energy is spent to deform the projectile (10–15%) and a vast amount is taken by the ejected ceramic debris [6,7]. Upon the impact of a projectile on a ceramic–composite armor compressive stress/shock wave propagates through the ceramic and reflects back as tensile wave from the ceramic–backing plate interface [8,9]. The amplitude of reflected tensile

---

\* Corresponding author.

E-mail address: gama@ccm.udel.edu (B.A. Gama).

**Nomenclature**

$x, y, z$	global co-ordinates
1, 2, 3	material co-ordinates
$w$	displacement in the $z$ -direction
$t$	time
$c_d$	dilatational wave speed
$P$	amplitudes of stresses
$L$	thickness of a plate
$\sigma$	normal stress
$\tau$	shear stress
$j$	1, 2, 3, ..., $n$
$k$	i, ii, iii, ...
$\bar{\sigma}$	normal stress in Laplace transformed domain
$s$	variable in Laplace transformed domain
$E$	Young's modulus
$E_u$	Young's modulus of foam before compaction
$E_c$	Young's modulus of foam after full compaction

$i$	1, 2, 3
$G$	shear modulus
$G_u$	shear modulus of foam before compaction
$G_c$	shear modulus of foam after full compaction
$m$	12, 23, 31
$v$	relative volume
$v_f$	relative volume of fully compacted foam
$\alpha$	parameter
$\beta$	hardening parameter
$\rho$	density
$\nu$	Poisson's ratio
$\sigma_y$	yield stress
$E_t$	tangent modulus
$X_i^C$	strength in direction $i$ under compression
$X_i^T$	strength in direction $i$ under tension
$S_m$	strength in direction $m$ under shear

wave depends on the impedance mismatch with the backing plate and plays a major role in ceramic fracture [10]. The fracture of ceramic creates fine ceramic particles ahead of projectile and flow of such comminuted ceramic particles can lead to high internal friction [11]. This phenomenon leads researchers to study the penetration behavior of confined ceramic [12–14]. “If a ceramic is well supported and protected from wave damage, it displays a high resistance to penetration by a long-rod projectile” and if confined in the impact face leads to interface defeat [13].

Numerical modeling of ceramic–metal armor is required to understand the penetration mechanisms. This requires constitutive modeling of ceramics and a good review is given by Rajendran et al. [15–17]. Cortez et al. [8] used a Lagrangian finite difference code to simulate the normal impact on ceramic armor backed by metallic plates without any frontal confinement. Their simulation predicted that once the ceramic is pulverized ahead of the projectile, the powder is pushed rather than

penetrating. Incorporation of Coulomb friction did not provide improvement in ballistic performance and the authors concluded that friction might be important for highly confined ceramic targets but not in their case. Rajendran [15] described the continuum mechanics based Rajendran–Grove ceramic model, which considers micro-crack initiation and growth in the ceramic in addition to elastic–plastic deformation. The micro-crack initiation is based on the generalized Griffith criterion and the damage growth is modeled by a state variable approach. Their simulation with EPIC-2 code produced realistic results and matched well with variety of experimental data. Wang et al. [18] implemented a ceramic model [2] in the explicit finite element code DYNA-2D and used the model to simulate their experiment on alumina ceramic–aluminum armor and found reasonable correlation. They identified four different deformation mechanisms of the aluminum backing plate (petalling, plugging, partial penetration and indentation) as a function of backing plate thickness. Navarro et al. [9] experimentally determined the trauma (maximum dynamic deflection) and energy absorbed as a function of areal-density (30–40 kg/m<sup>2</sup>) of ceramic–fiber-reinforced composite armor. They used alumina, boron carbide and silicon nitride ceramic tiles backed by aramid/vinyl ester or polyethylene/polyethylene composite and impacted those with 7.62 NATO projectiles. The trauma is found to be linearly decreasing and the energy absorbed linearly increasing with increase in armor areal-density.

Analytic models for armor design are developed in parallel with the development of lightweight armor. Florence [19] developed a model to determine the ballistic efficiency with the assumption that ceramic distributes the impact energy on the backing plate on a

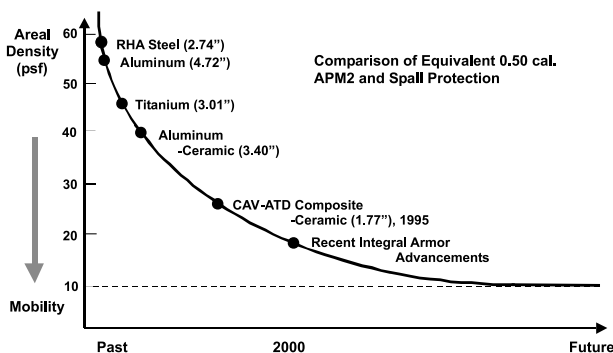


Fig. 1. Historical development of composite integral armor (arbitrary time axis).

larger area and the backing plate absorbs the energy through its deformation mechanisms, which was later reassessed by Hetherington and Rajagopalan [20]. Hetherington [21] described the optimization of two-component armor using Florence's model and later modified the Florence model for oblique impact [22]. Woodward [23] developed a model, which includes the projectile erosion, ceramic conoid formation, dishing failure of backing plate and perforation. Despite the simple model of Florence and the improvement made by Woodward, den Riejer [24] proposed more complex model incorporating the physics of projectile erosion, mushrooming and several damage process in the backing plate. Chocron et al. [25] recently proposed a model incorporating the physical processes involved in fabric, yarn and at composite levels. A good review on modeling of impact on fabrics and fiber-reinforced polymeric matrix composite is done by Navarro [26]. Analytical models incorporating ceramic tile, substrate and fabric backing can also be found in [27,28].

Study of two-component ceramic–metal and ceramic–fiber-reinforced composite armor can be found in literature; however, study of armor systems with three or more component is limited. Woodward et al. [29] found that an aluminum cover layer in addition to the aluminum backing plate results in greater overall ceramic fragmentation but less fragments being produced at the finer sizes compared with an unconfined target and the ceramic fragmentation decreases with the increase in its toughness. The effect of lateral/in-plane ceramic confinement (under biaxial compressive stress) without any cover has moderate effect on the irreversible deflection of the backing plate and number of radial cracks in the ceramic [30]. The performance of a three-component armor system involving ceramic strike face, with and without aluminum sandwich panel and S-2 glass/polyester composite is described by Senf et al. [31]. They used two different thickness of aluminum sandwich plate (20 and 50 mm) and two different projectiles (10-mm tungsten alloy cylinders and 12.7-mm armor piercing (AP)) to study the dynamic deflection as a function of time of the composite backing plate using a Craz–Schardin high-speed camera. The incorporation of an aluminum sandwich plate is found to reduce the dynamic deflection and ballistic resistance of the armor in the case of tungsten projectile. While the dynamic deflection is reduced with increasing sandwich thickness, no influence of sandwich panel on the ballistic resistance is found in the case of AP projectiles. The decrease in ballistic resistance is attributed to reduced efficiency of ceramic, because the sandwich panel does not provide support to the ceramic as the composite backing plate. One successful composite integral armor (CIA) developed by United Defense Limited Partnership (UDLP) for the US Army is a hybrid material system consisting of a ceramic strike face, a thin rubber layer and an S-2

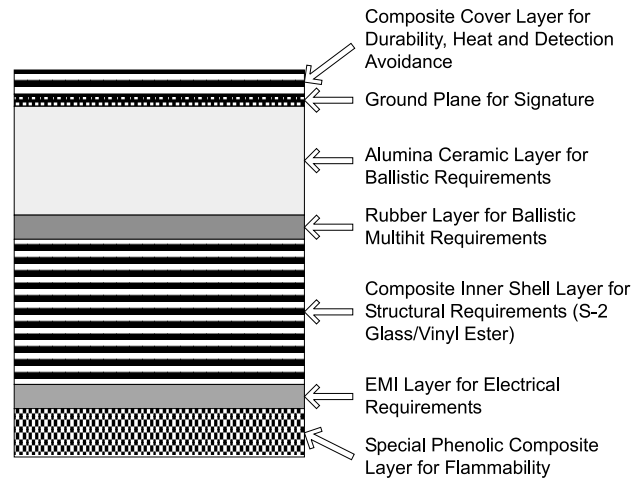


Fig. 2. Components of composite integral armor structure.

glass-based composite backing plate (Fig. 2) [32]. This armor is required to provide ballistic protection and structural integrity at minimal areal-density. Most CIA configurations utilize a rubber layer between the ceramic tile layer and the composite backing plate to increase the armor's multi-hit capability and structural damage tolerance [33,34]. Experimental evidence shows that an increase in rubber layer thickness decreases the dynamic deflection of the composite backing plate [35]. One-dimensional numerical stress wave experiments revealed that rubber delays the stress wave transfer and reduces the amplitude of transmitted stress wave to the backing plate [35]. The experimental and numerical results point to the importance of managing stress wave propagation in CIA during ballistic impact. However, rubber is a compliant material and reduces the structural stiffness of the armor. Hence, an optimal rubber layer thickness that balances the ballistic and structural performance at minimal weight should be determined to meet the specific mission requirements for a vehicle. Closed-cell aluminum foam is an alternative material to the rubber layer that has the potential to improve structural stiffness and ballistic properties.

In the present study, we describe the stress wave experiment through closed-cell aluminum foam, which shows the potential of this material in delaying and attenuating the propagating stress waves. We also present the numerical stress wave propagation models, novel design concepts, manufacturing and ballistic testing of a new generation of CIA incorporating a closed-cell aluminum foam layer.

## 2. Closed-cell aluminum foam and stress wave experiment

A variety of foaming processes and properties of closed-cell aluminum foam have been reported in the

literature [36–40]. However, the foaming process via a powder metallurgy route produces a solid skin, which may be of interest especially for the surface bonding of another material, has high specific strength, and unique non-linear compressive behavior [41]. Fig. 3 shows the quasi-static engineering stress–strain behavior of such closed-cell aluminum foam of different densities ( $\text{gm}/\text{cm}^3$ ). The flow stress of the foam is a strong function of foam density and the stress–strain curves can be divided into three regions: (1) linear elastic region, (2) collapse region and (3) densification region. In Region 1, the only deformation that occurs is elastic and is due to cell wall bending. This is followed by Region 2 in which plastic collapse of the first cell wall occurs and the stress drops. In Region 3, the foam progressively collapses and densifies. It was observed that deformation in Region 3 was highly localized and proceeded by the advance of a densification front from deformed to un-deformed regions of the sample. It has also been found that such type of aluminum foams is essentially strain rate independent [41,42]. Hence the quasi-static properties of aluminum foam presented in Fig. 3 are used in our numerical simulations.

Ballistic targets with and without aluminum foam were designed and tested to compare the shock wave propagation through the aluminum foam (Fig. 4(a) and (b)). The target without aluminum foam had an areal-density of  $161.03 \text{ kg}/\text{m}^2$  (32.98 psf) and the target with aluminum foam had an areal-density of  $157.75 \text{ kg}/\text{m}^2$  (32.31 psf). High hardness steel (HHS), aluminum foam, alumina ceramic ( $\text{Al}_2\text{O}_3$ ), and 7039 aluminum plates are bonded together with a thin layer of fast setting epoxy adhesive. Piezoresistant stress gages (Dynasen Model Mn/Cn 4-50-EK) are sandwiched between two ceramic layers to monitor the dynamic stress through the ceramic layer. These gages consist of two separate inter-laced 50- $\Omega$  foil grids enclosed in a polyamide plastic film.

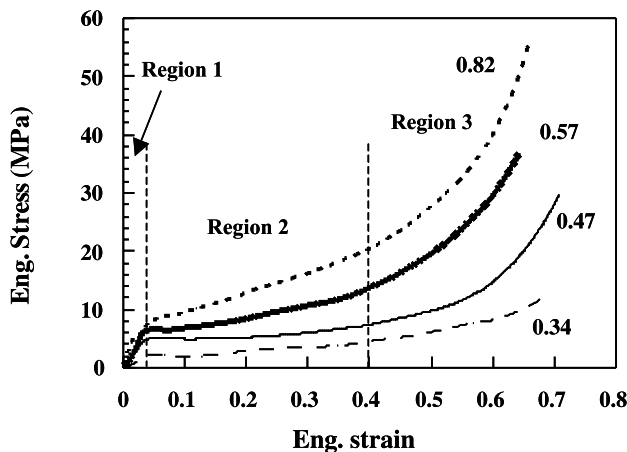


Fig. 3. Quasi-static stress–strain behavior of closed-cell aluminum foam. Numbers on the figure represents foam density in  $\text{gm}/\text{cm}^3$ .

One of the grids is made of manganin and is used to measure stress. The other is made of constantan and is used to measure lateral strain. Both grids are 6.35-mm square and 0.127-mm thick. The measured strain is used to correct the stress measurements. The gages are connected to a Dynasen CK-15-300 power supply and bridge circuit, which is triggered upon projectile impact by a ‘make’ screen with a simple capacitor discharge circuit. The signals from the gages are recorded on a digital oscilloscope. Calibration and data reduction of the stress gage signals are performed using software described by Franz and Lawrence [43]. Both the targets are impacted with 20-mm FSPs at a nominal impact velocity of 1067 m/s. The stress gage measurements are presented in Fig. 4(c). The rise time of the signal without foam is about  $1.0 \mu\text{s}$  and with foam is about  $2.0 \mu\text{s}$ . The maximum stress level attained in both the experiments is about 6.25 GPa. The incorporation of 12.7-mm aluminum foam delayed the stress signal about  $14.6 \mu\text{s}$  to reach the gage location. We have developed a one-dimensional plane strain finite element model of these experiments (detail of the model described in the following section) and have obtained about  $18.5 \mu\text{s}$  delay in the stress wave arrival with an impact velocity of 500 m/s (Fig. 4(c)). The finite element prediction also shows a

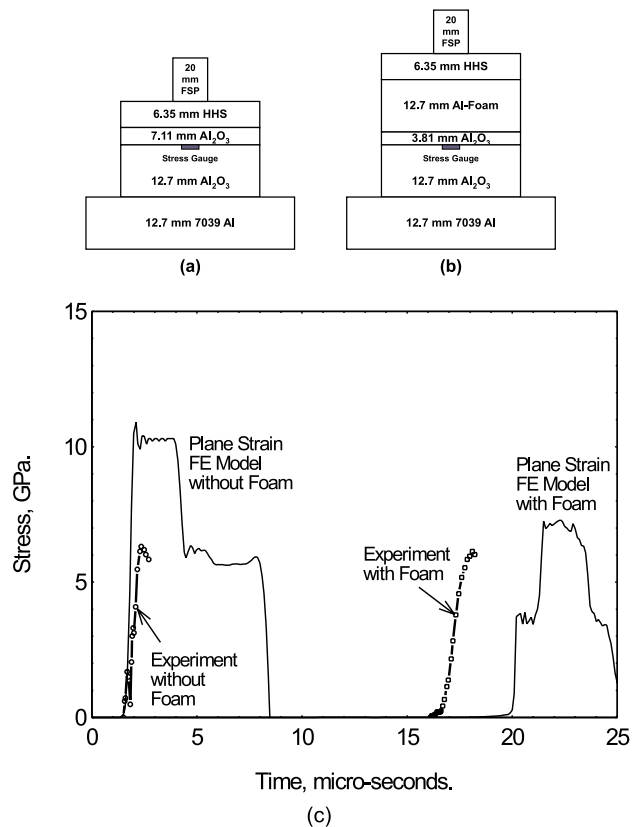
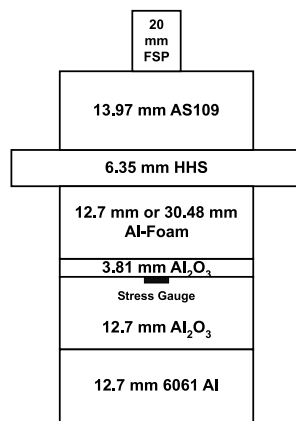


Fig. 4. Stress wave experiment with and without aluminum foam: (a) target without aluminum foam; (b) target with aluminum foam and (c) response of the stress gages and plane strain finite element predictions.

two-step rise in stress in the case of target with aluminum foam. The stress waves generated in the experiments are a combination of spherical dilatation, spherical shear and planar shear wave fronts. However, the plane strain model only produces planar dilatation and is not an exact model of the experiment. It is expected that the plane strain finite element will not match the three-dimensional experimental results, however, the finite element model predictions capture both the widening in rise time and delay in stress wave arrival. The experimental and finite element results identified two important characteristics of aluminum foam under stress wave propagation: (1) aluminum foam increases the rise time of the propagating stress wave and (2) incorporation of aluminum foam introduces a significant delay in stress wave propagation. In order to determine the effect of aluminum foam thickness, a second set of experiments are conducted.

The second set of stress wave experiments deals with two ballistic targets with different aluminum foam thickness (12.7 and 30.48 mm) and is shown in Fig. 5(a). An additional ceramic matrix composite layer (AS109, particulate SiC in  $\text{Al}_2\text{O}_3$  matrix with a small amount of

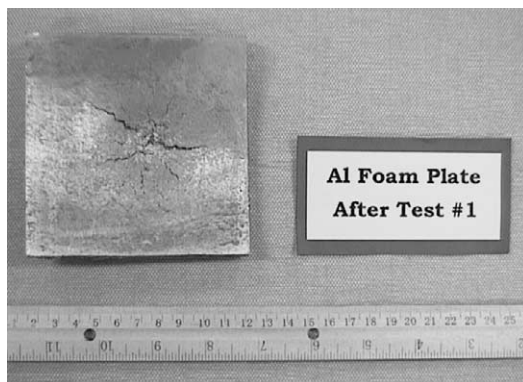
aluminum, made by Lanxide Armor Products) is bonded with the target described in Fig. 4(b). The nominal impact velocity of a 20-mm FSP was 915 m/s. The projectile impact on the first target (Test #1, with 12.7-mm aluminum foam) shattered the AS109 ceramic (Fig. 5(b)), deformed the HHS plate, and densified the aluminum foam (Fig. 5(c)). The stress gage recorded a stress pulse with the maximum stress amplitude of about 0.825 GPa. Impact on the second target (Test # 2, with 39.48-mm aluminum foam) showed similar fracture of AS109 ceramic and similar deformation of the HHS plate. However, the aluminum foam is partially densified but not completely (cross-section, Fig. 5(d)), and the stress gage did not record any signal. The major conclusion from these two experiments is that if the foam is not completely densified across the entire layer thickness, it will not allow any measurable stress waves to pass through. The air/gas filled cellular structure of the aluminum foam makes the stress wave propagation difficult. The cell wall acts as tiny wave-guide and dispersion of stress waves takes place. The deformation of closed-cell foam occurs by cell wall buckling and plastic collapse, which leads to localized densification. The



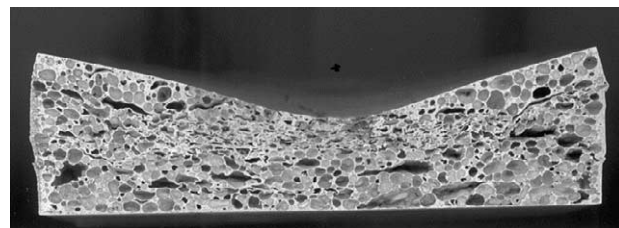
(a)



(b)



(c)

Al Foam Plate  
After Test # 2

(d)

Fig. 5. Stress wave experiment with different foam thickness: (a) target with aluminum foam and stress gage location; (b) fracture of AS109 ceramic strike face; (c) deformation of aluminum foam after Test # 1 and (d) cross-section of the deformation of aluminum foam after Test # 2.

deformation and densification originates from the point of applied load and propagates in the direction perpendicular and transverse to the applied load. Effective stress wave propagation can thus only occur when the closed-cell foam is completely densified. If the stress wave cannot reach the backing plate until the foam is completely densified, then the deformation and damage growth in the backing plate is delayed and the foam has potential to improve the ballistic efficiency of the armor. A detailed finite element analysis of one-dimensional plane strain stress wave propagation in multi-layer foam integral armor is presented next.

### 3. Stress wave propagation in aluminum foam integral armor

One-dimensional plane strain stress wave propagation in CIA and the effect of non-linear EPDM rubber layer thickness have been discussed by Gama et al. [35,44] and impact-induced stress wave propagation in such armor system is described by Mahfuz et al. [45]. One-dimensional plate impact produces planar dilatational stress wave propagation in both the projectile and target. On the other hand, the impact of a three-dimensional projectile (e.g., FSP) on a multi-layer thick armor plate produces three-dimensional spherical dilatational, spherical shear and planar shear wave fronts. Since the dilatational wave speed is higher than the shear wave speed, the through-thickness stress wave propagation in the impact centerline can be assumed planar and our analyses are valid only in this region. The through-thickness and impact direction is assumed aligned with the coordinate axis  $z$  (3), and the in-plane axes are denoted by  $x$  and  $y$  (1 and 2). The rubber layer of the integral armor is replaced with an aluminum foam layer. The signature layer is not modeled and the electro-magnetic and phenolic layers (Fig. 2) are lumped into the composite backing plate. The individual layers are assumed perfectly bonded to each other. The thickness of the steel impact plate (5 mm), composite cover layer (2.54 mm, 4 layers, [0/90]<sub>2</sub>, 24 oz/sq yards plain weave S-2 glass/vinyl ester), ceramic layer (17.78 mm, AD-90), and the composite backing plate (14.15 mm, 22 layers, [0/90]<sub>11</sub>, 24 oz/sq yards plain weave S-2 glass/vinyl ester) is kept constant throughout the analyses. The aluminum foam layer thickness is varied between 12.7 and 25.4 mm. This combination of layer thickness represents an integral armor of areal-density of about 97.65 kg/m<sup>2</sup> (20 psf).

The governing differential equations for plane strain wave propagation in a multi-layer CIA with linear-elastic material layers (Fig. 6) are given by

$$\frac{\partial^2 w_j}{\partial z_j^2} = \frac{1}{c_{dj}^2} \frac{\partial^2 w_j}{\partial t^2} \quad (1)$$

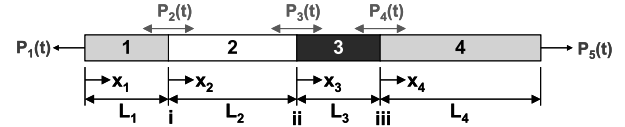


Fig. 6. Schematic of plane strain wave propagation through a multi-layer plate similar to integral armor construction.

with the boundary conditions

$$\begin{aligned} E_j \frac{\partial w_j(z_j, t)}{\partial z_j} \Big|_{z_j=0} &= P_j(t), \quad E_j \frac{\partial w_j(z_j, t)}{\partial z_j} \Big|_{z_j=L_j} \\ &= P_{j+1}(t), \end{aligned} \quad (2)$$

the initial conditions

$$w(z_j, 0) = \frac{\partial w_j(z_j, t)}{\partial t} \Big|_{t=0} = 0 \quad (3)$$

and the displacement and stress continuity conditions at the interfaces.

$$\begin{aligned} w_k(L_k, t) + w_{k+1}(0, t) &= 0, \\ \sigma_{zk}(L_k, t) + \sigma_{z(k+1)}(0, t) &= 0. \end{aligned} \quad (4)$$

The solutions to the above system of equations in the Laplace transformed domain are given by

$$\begin{aligned} \bar{\sigma}_j(w_j, s) &= P_j(s) \left\{ \sinh \left( \frac{s(L_j - w_j)}{c_{dj}} \right) \right\} / \left\{ \sinh \left( \frac{sL_j}{c_{dj}} \right) \right\} \\ &+ P_{j+1}(s) \left\{ \sinh \left( \frac{sL_j}{c_{dj}} \right) \right\} / \left\{ \sinh \left( \frac{sL_j}{c_{dj}} \right) \right\}, \end{aligned} \quad (5)$$

which can be transformed in the time domain by numerical Laplace inverse transformations. The above equations are only valid for linear-elastic material behavior.

In order to incorporate the non-linear deformation behavior of aluminum foam, an explicit non-linear dynamic finite element code LS-DYNA 940 is used [46,47], which is capable of solving a wide variety of problems including wave propagation, impact and penetration. In explicit dynamic analysis, the principal of virtual work is used to write a weak form of equilibrium equation incorporating the tractions and boundary conditions (For detail, see [46]) for each element. This is later summed up over all elements and integrated to obtain the solution for element accelerations. From the explicit solution of elemental acceleration, nodal velocity and displacements are obtained through integration. Once the displacements are known, incremental strains are computed to update the stress increment through material models and equation of states.

In the present finite element model, eight-node solid elements are used. Boundary conditions representing four axes of symmetry are included in the model to simulate the plane strain condition (Fig. 7) such that the

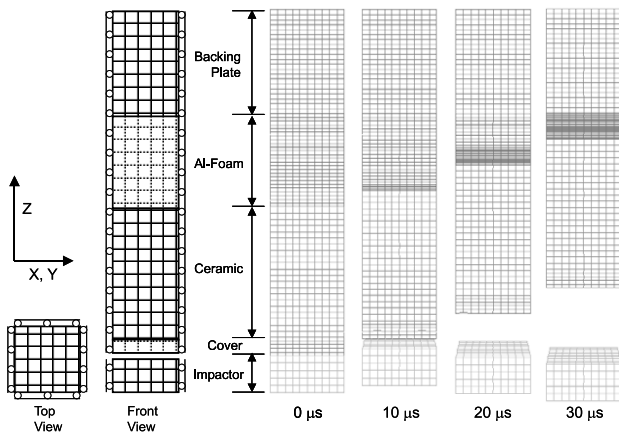


Fig. 7. Plane strain finite element model of aluminum foam integral armor and the dynamic deformation of the aluminum foam layer.

stress wave propagation is limited to through-thickness direction only. The  $X$ – $Y$  plane contains 100 elements ( $10 \times 10$ ), while the number of elements is chosen according to the thickness of the layer with a minimum of five elements through-thickness. The cover, ceramic, foam and the backing plate have 5, 21, 25 and 21 elements through-thickness, respectively.

Linear elastic material properties are used to model the impact plate, cover layer, ceramic layer, and the composite backing plate. Two material constants,  $E$  and  $\nu$  are required to model linear-elastic material behavior and are given in Table 1. The aluminum foam is modeled with the MAT\_HONEYCOMB material model of LS-DYNA 940, and the properties are extracted for foam density 0.57 gm/cc from Fig. 3 and are presented in Table 1. The MAT\_HONEYCOMB model [47] treats the material as orthotropic before compaction and the stress tensors are uncoupled with zero Poisson's ratio. The normal and shear load–displacements in each directions are input as load curves. Often the shear responses are not available and it is assumed that  $\tau = \sigma/2$  [48]. However, Chou [48] showed that an elastic–perfectly plastic model could give the shear responses. In our present analysis  $\tau = \sigma/2$  relation is used. The elastic moduli of the compacted material linearly increases up

to their fully compacted moduli with respect to relative volumes.

$$E_i = E_{ui} + \alpha(E_c - E_{ui}), \quad (6a)$$

$$G_m = G_{um} + \alpha(G_c - G_{um}), \quad (6b)$$

$$\alpha = \max \left[ \min \left( \frac{1 - v}{1 - v_f}, 1 \right), 0 \right]. \quad (6c)$$

The relative volume  $v$ , is defined as the ratio of the current volume to the initial volume. Typically, the initial volume is considered unity at the beginning of the computation. After full compaction to final volume  $v_f$ , the material is treated as elastic–perfectly plastic. The detail of stress update equations can be found in [47]. As our analysis is one-dimensional, it requires the input of through-thickness compressive load–displacement curve and the shear response is estimated from that. The impact velocity of the steel plate is varied between 250 and 750 m/s. A perfect surface-to-surface contact of projectile and armor without friction is assumed. The stress wave propagation in the aluminum foam armor is compared to armor without foam.

Fig. 7 shows the deformation of aluminum foam layer at different time intervals when impacted at 500 m/s. The plastic collapse and densification of foam starts at the impact side while the rest of the material remains elastic. It takes about 30  $\mu$ s for the complete densification of 12.7-mm aluminum foam. The stress wave propagation in the individual layers is a function of material properties and layer thickness. The dynamic response ( $\sigma_z$ ) at mid thickness of the individual layers is presented in Fig. 8 as a function of time (aluminum foam thickness = 12.7 mm, impact velocity = 500 m/s). Through-thickness normal stress ( $\sigma_z$ ) is made non-dimensional by the maximum compressive stress developed in the cover layer ( $\sigma_{z,cover}^{\max}$ ). The first compressive pulse in the cover layer is the input to the system. The stress in the cover layer becomes tensile as soon as the projectile bounces back from the target and the rest of the response is the reverberation of the input pulse and the interaction with the adjacent ceramic layer. The input pulse in the cover layer is transmitted to the ceramic

Table 1  
Material properties used in the one-dimensional finite element model

Material	Young's modulus, $E$ (GPa)		Poisson's ratio, $\nu$		Density, $\rho$ (kg/m <sup>3</sup> )	
Projectile	206.80		0.30		7850	
Cover	8.50		0.28		1783	
Ceramic	310.30		0.25		3500	
Backing plate	8.50		0.28		1783	
	$E_u$ (GPa)	$\rho$ (kg/m <sup>3</sup> )	Poisson's ratio of densified foam, $\nu_{\text{densified}}$	Yield stress, $\sigma_y$ (MPa)	Volume fraction of densified foam, $v_f$	Modulus of den- sified foam, $E_c$ (GPa)
Aluminum foam	0.177	470	0.285	241.40	0.29	68.97

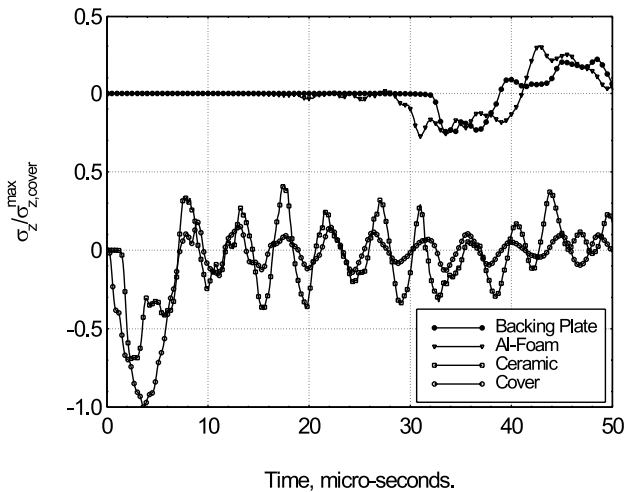


Fig. 8. Time-history of normal stress of individual CIA layers, aluminum foam thickness = 12.7 mm, impact velocity = 500 m/s.

layer through the cover/ceramic interface. The transmission and reflection coefficients can be estimated using one-dimensional wave propagation theory [10]. The response of the aluminum foam layer and the backing plate is presented with a coordinate shift in stress. The transmission and reflection coefficients in the ceramic–foam interface are 0.0173 and  $-0.9827$ , respectively, which means that most of the compressive stress pulse will be reflected as tensile stress in the ceramic–foam interface before the collapse of aluminum foam. After the collapse and densification of the aluminum foam layer ( $t > 26 \mu\text{s}$ ), significant stress rise and propagation is observed in both the aluminum foam and backing plate. The maximum amplitude of the stress pulse transferred into the backing plate is about 25% of the input in the cover layer.

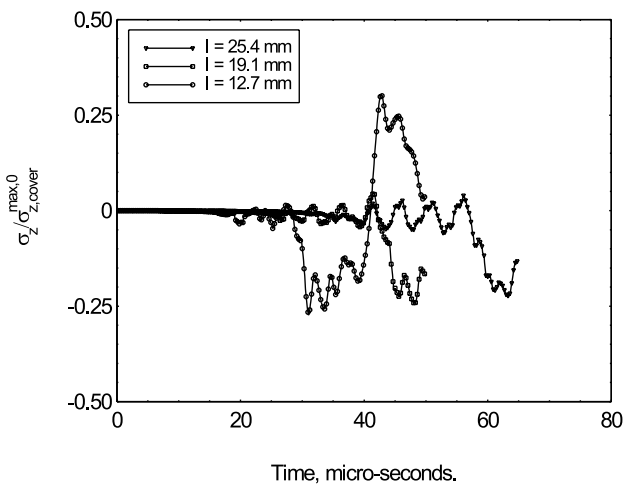


Fig. 9. Time-history of normal stress of aluminum foam layer as a function of foam thickness, impact velocity = 500 m/s.

The response of aluminum foam (impact velocity = 500 m/s) as a function of layer thickness,  $l$ , is shown in Fig. 9. Through-thickness normal stress ( $\sigma_z$ ) is made non-dimensional with the maximum normal stress at the cover layer for zero foam thickness ( $\sigma_{z,cover}^{max,0}$ ). The computation for foam thickness 12.7 and 19.1 mm was terminated at 50  $\mu\text{s}$  and for 25.4 mm at 65  $\mu\text{s}$ . The peak stresses are almost 25% of the input to the cover layer for all foam thicknesses. The arrival time of the stress pulse in the foam layer increases as a direct consequence of increased foam thickness and is related with the stress arrival at the backing plate (Fig. 10). The solid line represents the response of backing plate without any foam (Fig. 10(a)). The stress amplitude is found to decrease with the increase in foam thickness. The difference in the time of stress arrival to the backing plate with and without foam is termed as the time delay and increases with foam thickness. The peaks  $P$ ,  $Q$ , and  $R$  in Fig. 10(a) represent stress transfer to the backing plate after complete densification of the foam; however, a close-up shows earlier stress pulses ( $p$ ,  $q$ , and  $r$ ; Fig. 10(b)) before the densification of foam and is termed as elastic stress transfer. The maximum transmitted stress to the composite backing plate ( $\sigma_{z,bac}^{max}$ ) is made non-

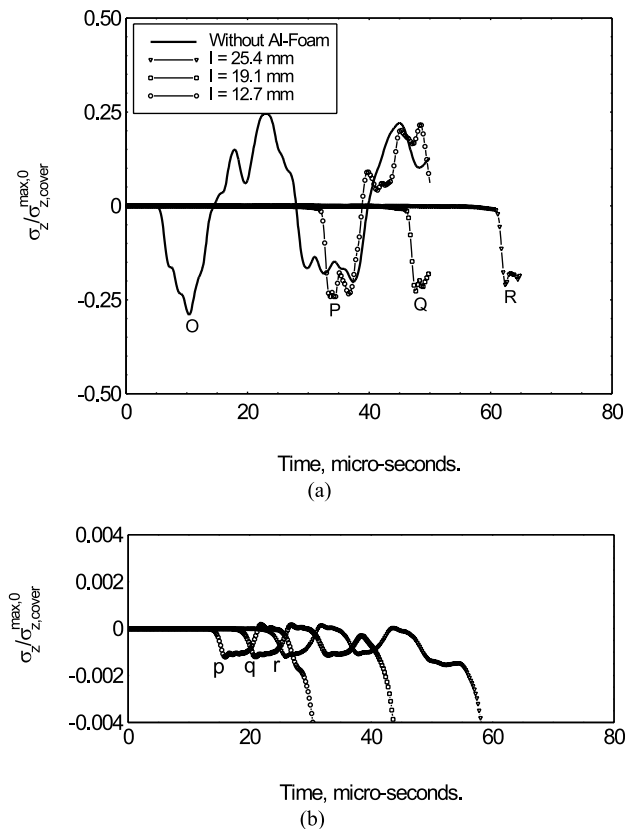


Fig. 10. Time-history of normal stress of the backing plate as a function of foam layer thickness, impact velocity = 500 m/s: (a) effect of foam thickness and (b) close-up of the response shows elastic response.



dimensional with that for zero foam thickness ( $\sigma_{z,bac}^{\max,0}$ ) and is presented in Fig. 11. The elastic stress transfer is less than 1% for all impact velocities studied. On the other hand, the stress transfer (for impact velocities 500 and 750 m/s) after complete foam densification linearly decreases at a rate of 1.1% per mm of foam thickness. The time delay of stress arrival in the backing plate is presented in Fig. 12 and is found to be increasing with foam thickness. The time delay of elastic pulse for all impact velocities is about 0.75  $\mu\text{s}/\text{mm}$ , however, the rate of time delay after foam densification decreases as impact velocity increases. These rates of delay are 2.16 and 1.42  $\mu\text{s}/\text{mm}$  for impact velocities 500 and 750 m/s. At impact velocities higher than 750 m/s, the rate of delay will approach the rate of delay of the elastic pulse (0.75  $\mu\text{s}/\text{mm}$ ). The composite backing plate in a CIA is multi-functional in nature, and contributes both in structural

and ballistic performance. It has been shown [35] that there will be one complete reverberation of stress wave (one forward traveling compression pulse and one backward traveling tensile pulse) in the backing plate ahead of the projectile if the impact velocity is less than 1220 m/s. Depending on the amplitude of the compressive stress pulse, micro-cracks will initiate in the composite and the tensile pulse will initiate interlaminar delamination. The incorporation of an aluminum foam layer between ceramic and composite backing might eliminate the stress wave-induced damages before the deformed projectile reaches the foam–composite interface by its time delay mechanism.

As stated earlier, the one-dimensional stress analysis is valid at the impact centerline without penetration in the armor. In the real impact event, the penetration event will follow the stress wave propagation and the wave front will be non-planar. In order to investigate the penetration event, a quarter-symmetric three-dimensional model of aluminum foam integral armor impacted by a 20 mm FSP is developed. The foam layer thickness is taken as 19.1 mm. To mimic the stress wave experiment done by Yu et al. [41], a thin layer of elastic–plastic material was incorporated in the model between the ceramic and aluminum foam layer. The initial impact velocity of the projectile is set to 900 m/s. The projectile and ceramic are modeled with MAT\_PLASTIC\_KINEMATIC and the backing plate is modeled with MAT\_COMPOSITE\_FAILURE\_SOLID material models [47] and the corresponding material properties required for the models are presented in Table 2. The MAT\_PLASTIC\_KINEMATIC is a bi-linear elastic plastic model with isotropic and kinematic hardening and needs five material properties ( $E$ ,  $\nu$ ,  $\sigma_y$ ,  $E_t$ , and  $\beta$ ).  $E_t$  is the slope of the bi-linear stress strain curve and  $\beta$  is the hardening parameter. The value of hardening parameter  $\beta$  is considered zero (kinematic hardening) in the present analysis. MAT\_COMPOSITE\_FAILURE\_SOLID is an orthotropic material model for solid elements with maximum stress failure criteria. Nine material constants and nine strength properties are required to define this model and are given in Table 2. Fig. 13 shows the sequence of projectile penetration and dynamic deformation of the aluminum foam. The solution is terminated after 63  $\mu\text{s}$  because the foam cells are compressed down to infinitesimal thickness and the time-step required for such solution is so small that it will take infinite time to solve the problem. The cross-sectional view of the deformed aluminum foam [41] is placed close to the numerical solution at 63  $\mu\text{s}$  to show that the deformation pattern obtained from the numerical simulation matches well with the experimental observation. The deformation pattern of the aluminum foam also suggests that if an aluminum foam plate is placed after the backing plate, it could contain the dynamic deflection of the armor.

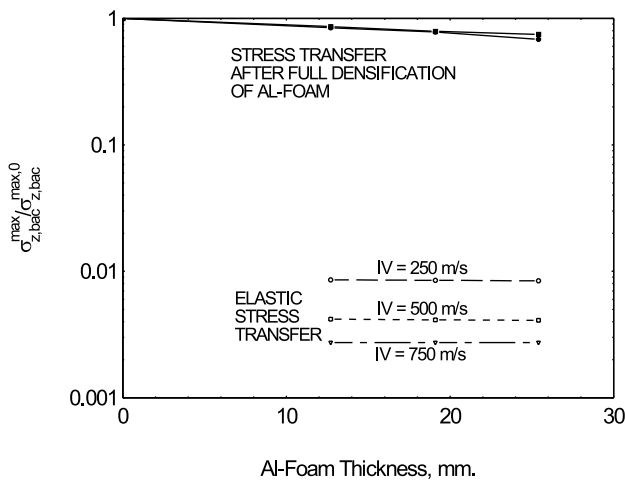


Fig. 11. Transmission of stress pulse in the backing plate as a function of foam thickness.

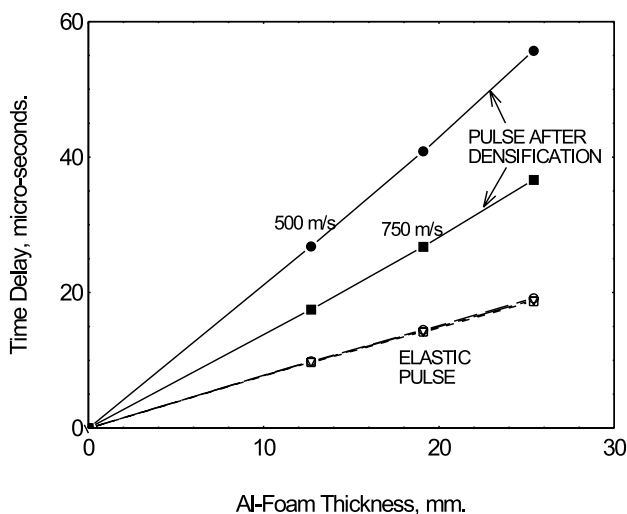
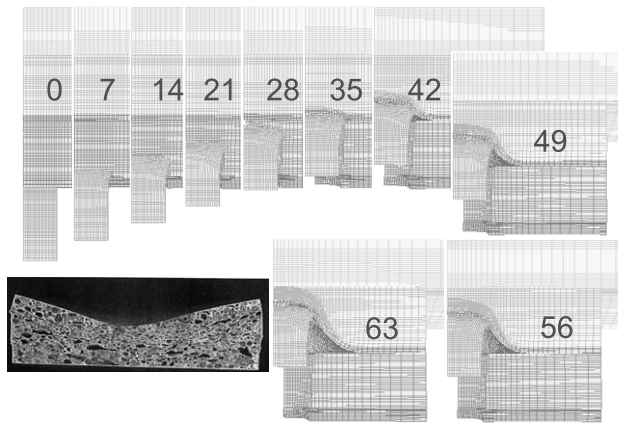


Fig. 12. Time delay in the stress wave arrival at the backing plate as a function of foam thickness.

Table 2

Material properties used in the three-dimensional finite element model

Material	$E$ (GPa)	$\nu$	$\rho$ (kg/m <sup>3</sup> )	$\sigma_y$ (MPa)	Tangent modulus, $E_t$ (GPa)	
FSP	206.91	0.285	7850	1069.1	2.0	
Cover	20.00	0.22	1783	200.0	15.0	
Ceramic	310.30	0.25	3500	3000.0	0.0	
Aluminum foam	$E_u$ (GPa)	$\rho$ (kg/m <sup>3</sup> )	$\nu_{\text{densified}}$	$\sigma_y$ (MPa)	$\nu_f$	$E_c$ (GPa)
	0.177	470	0.285	241.40	0.29	68.97
Backing plate	$\rho$ (kg/m <sup>3</sup> )	Modulus (GPa)	Poisson's ratio		Shear modulus (GPa)	
	1783	$E_{11}$	29.48	$\nu_{21}$	0.0085	$G_{12}$
		$E_{22}$	29.48	$\nu_{31}$	0.1145	$G_{23}$
Strength properties (MPa)		$E_{33}$	10.38	$\nu_{32}$	0.1145	$G_{31}$
		$X_1^C$	391.1	$X_1^T$	741.4	$S_{12}$
		$X_2^C$	391.1	$X_2^T$	741.4	$S_{23}$
		$X_3^C$	179.3	$X_3^T$	60.0	$S_{31}$

Fig. 13. Penetration and dynamic deformation of aluminum foam integral armor. Numbers indicate time in  $\mu\text{s}$ .

#### 4. Design of aluminum foam integral armor

Based on the stress wave experiment of Yu et al. [41] and the numerical simulation presented in Section 3, a test matrix has been developed (Fig. 14) to assess the potential benefits of using metal foams in an integral armor and to design the next generation integral armor to satisfy the Army requirements [1]. Three different designs of integral armor with metal foam have been proposed. These designs represent unique functionality of the aluminum foams in the integral armor. The rubber layer of the baseline CIA (Fig. 14(a), Baseline) has been simply replaced by the aluminum foam (Fig. 14(b), Design 1) to eliminate any relative rotational d.o.f between ceramic and backing plate, to improve structural stiffness of the armor, and to attenuate the stress wave propagation. The next design (Fig. 14(c), Design 2) includes an additional aluminum foam backing plate to minimize dynamic deflection. The last design (Fig. 14(d),

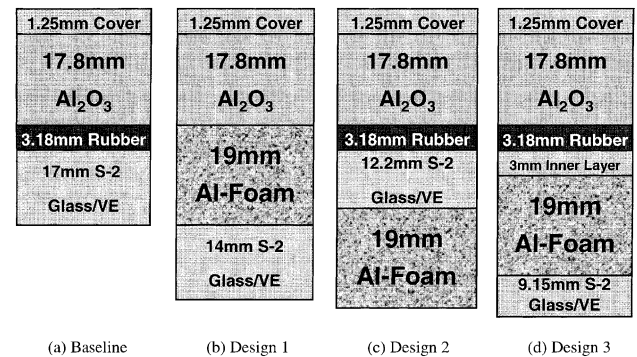


Fig. 14. Innovative design of aluminum foam integral armor.

Design 3) uses a rubber layer and a thin composite inner layer to distribute the load over a greater region on the metal foam. The material system and individual layer thickness is marked in Fig. 14. All designs have the same areal-density 97.65 kg/m<sup>2</sup> (20 lb/ft<sup>2</sup>) as the baseline composite integral armor. The thickness of the cover layer and the ceramic layer is kept constant for all design cases. The foam thickness is also kept constant at 19.00 mm to minimize the production cost of foam panels. If rubber is used in the foam armor panels, the thickness is chosen to be the same as the baseline. The only parameter varied to keep the areal-density constant is the composite backing plate thickness.

#### 5. Multi-step processing of armor panels

A total of four-baseline armor panels and one of each aluminum foam CIA configuration is manufactured using a multi-step manufacturing technique. This method is presented in Fig. 15. The composite backing plates of different thickness are processed using vacuum-

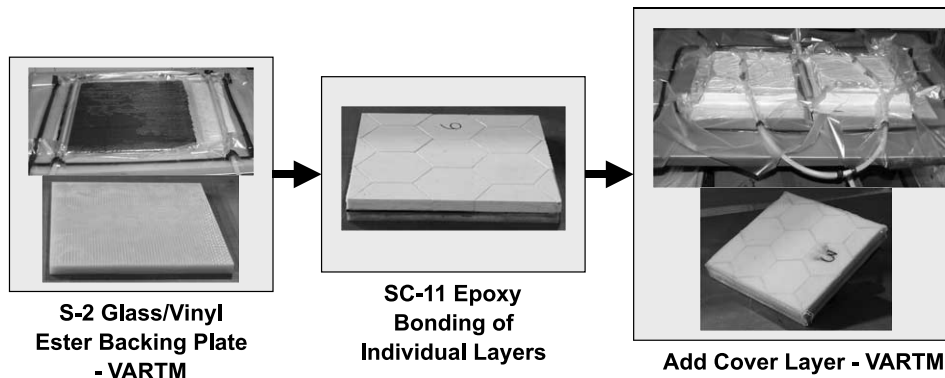


Fig. 15. Multi-step processing of integral armor.

assisted resin transfer molding (VARTM). Details of the VARTM process can be found in [49]. Plain weave S-2 glass fabric (24 oz/sq yards) with 365 sizing is used to make the preforms. The preforms are infused with vinyl ester 411–C50 resin and cured at room temperature and post-cured at 121°C (250°F) for 3 h. The S-2 glass/vinyl ester panels are then machined to 305 mm × 305 mm size. EPDM rubber sheets of same size are washed with soap and water, dried, and a thin coating of LORD 7701 primer is applied on both sides. Closed-cell aluminum foam panels of nominal density 500 kg/m<sup>3</sup> and of dimension 101.6 mm × 101.6 mm × 19.0 mm were fabricated. The foam panels are cleaned with distilled water and dried at room temperature. A solution containing 10% glycidoxo (epoxy) functional methoxy silane (Dow Corning® Z-6040) is prepared with de-ionized water. Acetic acid is added to the solution to maintain pH in the range 3.5–4.0. The aluminum foam panels are then soaked into the silane solution and oven-dried for 1 h at 90°C. Hexagonal ceramic tiles (AD-90) are cleaned with compressed air. Non-hexagonal ceramic pieces required making a 305 mm × 305 mm square array of tiles is cut from the hexagonal tiles using a slot grinder. Fishing lines are cut into small pieces and bonded with spray-adhesive on the sides of the ceramic tile to ensure a gap between adjacent tiles. The next step is to bond the individual layers with SC-11 epoxy resin. A wooden frame is made to hold all the layers together. A peel ply is used to avoid contact between the wooden mold and the part. The backing plate is first placed on the wooden frame. A thin layer of epoxy resin is then evenly distributed on top. To control the bond-line thickness, a glass scrim cloth (0.125 mm thick) is placed on the backing plate. More resin is added on top of the scrim cloth. The rubber (or aluminum foam) layer is laid next. On top of the rubber layer, resin and scrim cloth are placed to bond the next layer (ceramic layer or any successive layer). Once the hand lay-up of all layers is completed, the assembly is placed in a vacuum bag with sufficient breather material to absorb the excess epoxy resin. The

vacuum bag is then placed inside an oven and the part is cured at 121°C (250°F) for 2 h and at 149°C (300°F) for another 2 h under vacuum. Once the cure is complete the part is slowly cooled in the oven under vacuum. This armor plate is then covered with two layers of S-2 glass fabric and VARTM processed with vinyl ester 411–C50 resin at room temperature to obtain the cover layer. The complete integral armor is then post cured at 121°C (250°F) for 3 h.

## 6. Ballistic test results and discussion

Integral armor panels are impacted with 20-mm FSP projectiles. Previous research suggested that a 20-mm FSP with impact velocity of 838 m/s (2750 ft/s) would defeat a 97.6 kg/m<sup>2</sup> (20 lb/ft<sup>2</sup>) CIA without penetrating the backing plate [33,34]. Accordingly, all the impact tests were conducted at a nominal impact velocity of 838 m/s.

Dynamic deflection of the back-face of the armor under incomplete/partial penetration is a critical performance metric [1]. The integral armor panels were mounted on a thick backing of plasticine clay before projectile impact. The dynamic deformation of the back-face of the armor is engraved in the plasticine clay after the impact event. This dynamic deflection is then measured as a function of radial location and is presented in Fig. 16 for all the tests done. Dynamic deflection of the baseline CIA is presented with the error bars from four test specimens. The curve has a bell shape with a peak at about 32 mm (1.25 in.) and a span diameter of about 200 mm (8.0 in.). Design 1 has a dynamic deflection contour, which shows less deflection over the whole span as compared to the baseline, which is somehow similar to the findings of Sherman [30]. Design 2 has the least dynamic deflection among all the armor panels tested. Design 3 has higher deflection in the central region but less over the rest of the span as compared to the base

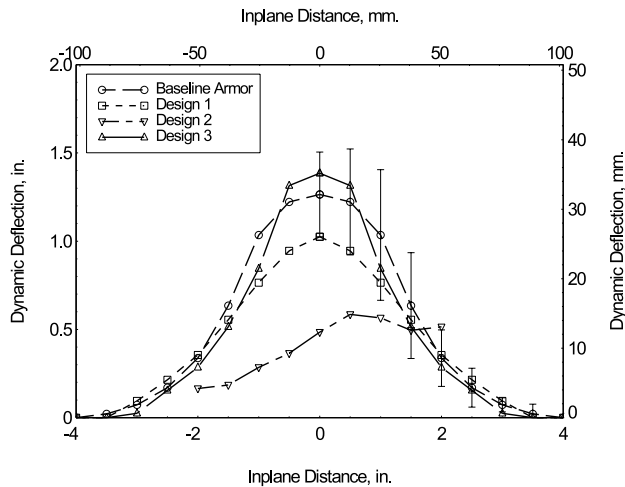


Fig. 16. Dynamic deflection of aluminum foam integral armor.

line. These observations will be correlated with the deformation and damage profile presented in Fig. 17.

The armor panels after the ballistic impact is carefully removed from the test fixture such that all the fractured ceramic is contained in the impact cavity other than material ejected during the impact. The impact cavity is then filled with vinyl ester resin to hold the broken ceramic pieces in place. The armor panels are then sectioned, polished, and pictures are taken with a digital camera. These pictures are shown in Fig. 17, and provide us the information on deformation, damage, and relative comparisons between them. The extent of delamination in the backing plate is marked with a polygon on the picture. The baseline armor (Fig. 17(a)) shows severe ceramic fracture; cover push-out, penetration through rubber, and the largest volumetric delamination of the backing plate. The load distribution by the fractured ceramic particles on the backing plate during impact is equivalent to one hexagonal tile area. A spring-back effect is observed in all armor panels such that the permanent (static) deformation of the back face is less than 10% of the maximum dynamic deflection. Debonding in the ceramic–rubber and rubber–composite interface is observed (not visible in figure) suggesting flexural bending of both the ceramic and composite layer.

The overall performance of Design 1 (Fig. 17(b)) is better than the baseline. The volumetric ceramic fracture is less than that of the baseline. Most of the ceramic particles are small and medium in size, and almost no pieces are larger than the particles observed in the baseline. The finer ceramic fracture is attributed to the low impedance between aluminum foam and ceramic [31]. Deformation of aluminum foam is of inverted bell shape and is localized. The densification of aluminum foam is localized under the projectile head and in a small surrounding area. Since there is no stress wave transfer

to the backing plate before the complete densification, the aluminum foam is acting as a stress wave filter. The deformation pattern of aluminum foam suggests that the load distribution on the backing plate is on a much smaller area than the baseline. The volumetric delamination of the backing plate is also less than the baseline, possibly due to a significant decrease in premature damage due to stress wave propagation before the arrival of the projectile. Debonding between the foam–composite interface is observed, however, there is almost no debonding in the ceramic–foam interface suggesting flexural bending limited in the backing plate only. It was demonstrated earlier (Fig. 16) that the dynamic deflection of Design 1 is less than the baseline suggesting that the residual kinetic energy of the projectile pushing the backing plate is less than that of the baseline. Design 1 is thus proven to be a better armor solution than the baseline CIA solution with a rubber layer.

The comparison between Design 2 (Fig. 17(c)) and the baseline will be easier if we think that Design 2 is same as the baseline with added aluminum foam backing. The deformation pattern of the cover, ceramic and rubber layer is similar to the baseline. However, the volumetric delamination of the backing plate is less than the baseline and is comparable to Design 1. Debonding in the composite–foam interface is visible and the deformation pattern of the aluminum foam backing plate at the composite backing/aluminum foam interface is a representation of the dynamic deformation of the composite back face. The deformation of aluminum foam is mostly plastic. The dynamic deformation presented in Fig. 16 is the deflection of the back face of the aluminum foam, which we can see from Fig. 17(c) as a permanent deformation. The damage in the aluminum foam backing plate is distributed over the whole span of the armor plate, which suggests that if foam is used behind the composite backing plate a good bonding between these layers is not important.

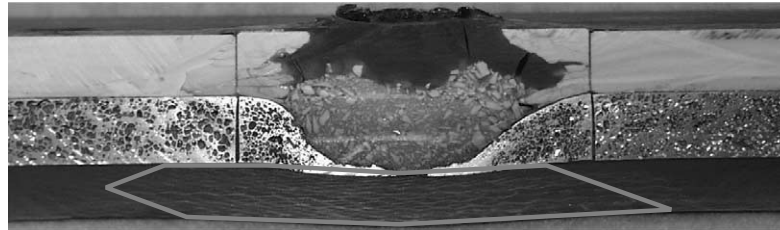
In Design 3 (Fig. 17(d)), the composite inner layer served the purpose of distributing the load over the aluminum foam. The ceramic fracture is similar to the baseline and we do not get the benefit of Design 1 in this configuration. Debonding is observed in almost all layer interfaces. Even though the volumetric delamination is least compared to all designs, its dynamic deflection similar to the baseline CIA suggests a poor design.

## 7. Summary

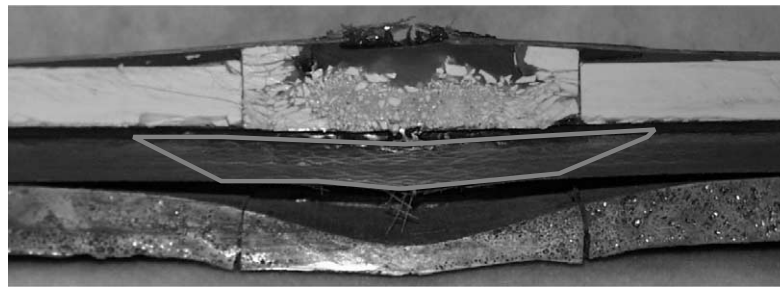
The unique capability of closed-cell aluminum foam in delaying stress wave propagation and attenuation is presented through experimental and numerical analyses. It has been found that the dynamic deformation of aluminum foam starts at the impact face and propagates through the thickness till complete densification. The



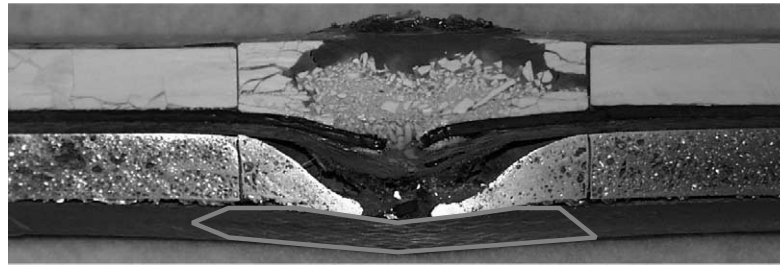
(a) Baseline



(b) Design 1



(c) Design 2



(d) Design 3

Fig. 17. Impact damage modes of the aluminum foam integral armor.

cellular structure of aluminum foam acts as tiny waveguides and geometric dispersion of stress waves takes place. Effective stress wave propagation through aluminum foam only occurs after complete densification. If the foam densification is partial it can act as a stress wave filter. The time required for complete densification appears as a time delay in stress transfer to the next layer (backing plate), and is found to be a linear function of foam thickness. The time delay in stress wave transfer to the composite backing plate is beneficial in delaying the micro-damage mechanisms, which might help in improving the ballistic performance of CIA. Aluminum foam is found to reduce the amplitude of the stress pulse transferred to the backing plate; however, the reduction is not significant. Based on the experi-

mental and numerical stress wave propagation results, three novel aluminum foam integral armor designs have been evaluated.

Various CIA panels have been ballistically tested under 20-mm FSP impact to assess the associated damage of baseline and aluminum foam integral armor. The relative study between three different aluminum foam armor designs and their comparison with the baseline gives insight into the performance and deformation behavior of this new class of aluminum foam-based CIA. In comparison to the baseline, Design 1 performed the best by providing better ceramic fracture, less cover separation, localized aluminum foam deformation, less dynamic deflection, less volumetric delamination of the backing plate, and no debonding in the

ceramic–foam interface. The superior performance of this novel aluminum foam integral armor is a step forward to lighter and more damage tolerant CIA for the next generation of armored vehicles.

## Acknowledgements

Prepared through participation in the Composite Materials Research Collaborative Program sponsored by the US Army Research Laboratory under Cooperative Agreement DAAL01-96-2-0048. Financial support for this work also provided by the Army Research Office (ARO), Grant Number DAAG55-98-K-0002.

## References

- [1] Fink BK. Performance metrics for composite integral armor. *J of Thermoplast Compos Mater* 2000;13(10):417–431.
- [2] Wilkins ML, Cline CF, Honodel CA. Fourth progress report of light armour program. Report UCRL 50694, Lawrence Radiation Laboratory, University of California; 1969.
- [3] Wilkins ML. Mechanics of penetration and perforation. *Int J Eng Sci* 1978;16:793–807.
- [4] Wilkins ML. Computer simulation of penetration phenomenon. In: Laible RC, editor. *Ballistic materials and penetration mechanics*. Amsterdam: Elsevier; 1980. p. 225–52.
- [5] Viechnicki DJ, Anctil AA, Papetti DJ, Prifty JJ. Lightweight armor – a progress report. US Army MTL TR 89-8; 1989.
- [6] Nicol B, Pattie SD, O'Donnell RG, Woodward RL. Fracture of ceramics in composite armors. In: *Fracture mechanics in engineering practice*. Melbourne University: Conference of Australian Fracture Group; 1988.
- [7] Woodward RL, O'Donnell RG, Baxter BJ, Nicol B, Pattie SD. Energy absorption in the failure of ceramic composite armours. *Materials Forum* 1989.
- [8] Cortes R, Navarro C, Martinez MA, Rodriguez J, Sanchez-Galvez V. Numerical modeling of normal impact on ceramic composite armours. *Int J Imp Eng* 1992;12(4):639–51.
- [9] Navarro C, Martinez MA, Cortes R, Sanchez-Galvez V. Some observations on the normal impact on ceramic faced armours backed by composite plates. *Int J Imp Eng* 1993;13(1):145–56.
- [10] Meyers MA. *Dynamic behavior of materials*. New York: Wiley; 1994.
- [11] Curran DR, Seaman L, Cooper T. Micromechanical model for comminution and granular flow of brittle material under high pressure and high strain rate: application to penetration of ceramic plates. Progress report of SRI to the Office of Naval Research, Contract No, N00013-88-C-0734; 1991.
- [12] Shockey DA, Marchand AH, Skaggs SR, Cort GE, Burkett MW, Parker R. Failure phenomenology of confined ceramic targets and impacting rods. *Int J Imp Eng* 1990;9:263–75.
- [13] Hauver GE, Netherwood PH, Benck RF, Kecskes LJ. Enhanced ballistic performance of ceramics. *Proc Army Sci Conf* 1994;4:1633–40.
- [14] Lundberg P, Renstrom R, Lundberg B. Impact of metallic projectiles on ceramic targets: transition between interface defeat and penetration. *Int J Imp Eng* 2000;24:259–75.
- [15] Rajendran AM. Modeling the impact behavior of AD85 ceramic under multiaxial loading. *Int J Imp Eng* 1994;15(6):749–68.
- [16] Rajendran AM, Dandekar DP. Inelastic response of alumina. *Int J Imp Eng* 1995;17:649–60.
- [17] Rajendran AM, Grove DJ. Modeling the shock response of silicon carbide, boron carbide and titanium diboride. *Int J Imp Eng* 1996;18(6):611–31.
- [18] Wang B, Lu G, Lim MK. Experimental and numerical analysis of the response of aluminum oxide tiles to impact loading. *J Mater Proc Tech* 1995;51:321–45.
- [19] Florence AL. Interaction of projectiles and composite armor plate II. AMMRG-CR-69-15. Menlo Park, CA, USA: Stanford Research Institute; 1969.
- [20] Hetherington JG, Rajagopalan BP. An investigation into the energy absorbed during ballistic perforation of composite armours. *Int J Imp Eng* 1991;11:33–40.
- [21] Hetherington JG. The optimization of two component composite armours. *Int J Imp Eng* 1992;12(3):409–14.
- [22] Hetherington JG, Lemieux PF. The optimization of two component composite armours. *Int J Imp Eng* 1994;15(2):131–7.
- [23] Woodward RL. A simple one-dimensional approach to modeling ceramic composite armour defeat. *Int J Imp Eng* 1990;9(4):455–74.
- [24] den Reijer PC. Impact on ceramic faced armor. Ph.D. Thesis, Delft, Delft University of Technology, The Netherlands; 1991.
- [25] Chocron IS, Benloulou V. A new analytical model to simulate impact onto ceramic/composite armors. *Int J Imp Eng* 1998;21(6):461–71.
- [26] Navarro C. Simplified modeling of the ballistic behavior of fabrics and fiber-reinforced polymeric matrix composites. *Key Eng Mater* 1998;141–143:383–400.
- [27] Walker JD, Anderson Jr CE. An analytic model for a ceramic tile, substrate, and fabric. In: 17th International Symposium on Ballistics, Midrand, South Africa; 1998.
- [28] Walker JD. Constitutive model for fabrics with explicit static solution and ballistic limit. Texas: San Antonio; 1999. p. 1231–8.
- [29] Woodward RL, Gooch Jr. WA, O'Donnell RG, Perciavalli WJ, Baxter BJ, Pattie SD. A study of fragmentation in the ballistic impact of ceramics. *Int J Imp Eng* 1994;15(5):605–18.
- [30] Sherman Dov. Impact failure mechanisms in alumina tiles on finite thickness support and the effect of confinement. *Int J Imp Eng* 2000;24:313–28.
- [31] Senf H, Strassburger E, Rothenhausler H. Investigation of bulging during impact in composite armor. *J Phys IV France* 1997;7:C3-301–6.
- [32] Composite structure design guide. Composite Armored Vehicle Program. United Defense L. P.; 1997–1998.
- [33] Fink BK, Gillespie Jr JW. Cost-effective manufacturing of damage tolerant integral armor. ARL Technical Report, ARL-TR-2319, September 2000.
- [34] Monib A, Gillespie Jr JW, Fink BK. Damage tolerance of thick-section composites subjected to ballistic impact. CCM Report, No. 99-08, University of Delaware; 1999.
- [35] Gama BA, Gillespie JW Jr, Mahfuz H, Bogetti TA, Fink BK. Effect of non-linear material behavior on the through-thickness stress wave propagation in multi-layer hybrid lightweight armor. In: *Proceedings of the International Conference on Comp Engineering and Science*, Los Angeles, CA, 2000 August, vol. I. p. 157–62.
- [36] Kenny LD. Mechanical properties of particle stabilized aluminum foam. *Mater Sci Forum* 1996;217–222:1883–90.
- [37] Yu CJ, Banhart J. Mechanical properties of metallic foams. In: *Proceedings of Fraunhofer USA Metal Foam Symposium*, Stanton, Delaware, 1997 October 7–8. p. 37–48.
- [38] Deshpande VS, Fleck NA. Isotropic constitutive models for metallic foams. Technical Report, University of Cambridge, CUED/C-MICROMECH/TR.9, ISSN 0309-7420; November 1998.
- [39] Deshpande VS, Fleck NA. High strain rate compressive behavior of aluminum alloy foams. *Int J Imp Eng* 2000;24(3):277–98.

- [40] Yu CJ, Eifert HH. Metal foaming by a powder metallurgy method: production, properties and applications. *Mater Res Innov* 1998;2:181–8.
- [41] Yu CJ, Eifert HH, Hall IW, Franz R, Leighton K. Feasibility study on deformation energy absorption of metal foams at high strain rates. FC-DE Report No. DAAG55-98-K-0002; November 1998.
- [42] Yu CJ, Claar TD, Eifert HH, Hall IW, Franz RE, Leighton KT, Hasson DF. Deformation energy absorption of metal foams at high strain rates. *Proc Met Foam* 1999;347–52.
- [43] Franz RE, Lawrence W. Stress measurements in glass during shaped-charge jet penetration. US Army Ballistic Research Laboratory Memorandum Report BRL-MR-3518; 1986.
- [44] Gama BA, Bogetti TA, Fink BK, Mahfuz H, Gillespie Jr JW. Study of through-thickness wave propagation in multi-layer hybrid lightweight armor. In: *Proceedings of the 13th ASC Ann Technical Conference*, Baltimore, MD, 1998 September 21–23. p. 1834–48.
- [45] Mahfuz H, Zhu Y, Haque A, Abutalib A, Vaidya U, Jeelani S, Gama B, Gillespie J, Fink B. Investigation of high-velocity impact on integral armor using finite element method. *Int J Imp Eng* 2000;24:203–17.
- [46] Hallquist JO. LS-DYNA3D theoretical manual. Rev. 2. Livermore, CA: LSTC; 1991.
- [47] LS-DYNA keyword user's manual. Version 950. Livermore, CA: LSTC; 1999.
- [48] Chou CC. Honeycomb material models for simulating responses of foams. In: *Proceedings of the Fifth International LS-DYNA Users Conference*, Southfield, MI; 1998.
- [49] Fink BK, Gillio EF, McKnight GP, Gillespie Jr JW, Advani SG, Eduljee RF, Bernetich KR. Co-injection resin transfer molding of vinyl-ester and phenolic resins. Army Research Laboratory Technical Report, ARL-TR-2150; December 1999.